INSTITUTE OF PHYSICS PUBLISHING JOURNAL OF MICROMECHANICS AND MICROENGINEERING

J. Micromech. Microeng. **15** (2005) 1344–1361 doi:10.1088/0960-1317/15/6/028

Transient flow pattern based microscale boiling heat transfer mechanisms

Jinliang Xu, Sheng Shen, Yunhua Gan, Yuxiu Li, Wei Zhang and Qiucheng Su

Micro Energy System Laboratory, Guangzhou Institute of Energy Conversion, Chinese Academy of Sciences, Wushan, Nengyuan Road, Guangzhou 510640, People's Republic of China

E-mail: xujl@ms.giec.ac.cn

Received 31 January 2005, in final form 22 March 2005
Published 16 May 2005
Online at stacks.iop.org/JMM/15/1344

Abstract

In our previous paper (J L Xu *et al* 2005 *J. Micromech. Microeng.* **15** 362–76), it is identified that the transient flow patterns for microscale boiling heat transfer are repeated on the timescale of milliseconds. A full cycle could be subdivided into three substages: liquid refilling stage, bubble nucleation, growth and coalescence stage and transient annular flow stage. Five heat transfer mechanisms could be deduced from the transient flow patterns. This paper extends the above work and mainly focuses on the boiling heat transfer behavior, which was performed for 102 runs with the following data ranges: inlet pressures of 1–2 bar, inlet liquid temperatures of 24–45 °C, pressure drops of 10–100 kPa, mass fluxes of 64–600 kg m^{-2} s^{-1}, heat fluxes of 150–480 kW m^{-2}, exit vapor qualities of 0.07–1.15 and the boiling numbers of 0.69×10^{-3}–5.046×10^{-3}. The silicon wafer test section consists of ten triangular microchannels with the hydraulic diameter of 155.4 μm. Acetone is selected as the working fluid. The heat transfer coefficients were analyzed with the effects of the heat fluxes, the mass fluxes and the vapor mass qualities. We provide a link between the transient flow patterns and the heat transfer process. The boiling numbers can be used to characterize the microscale boiling heat transfer, which can display three distinct regions by dividing the boiling numbers into three subranges. The transient flow pattern based heat transfer mechanisms are very consistent with the heat transfer coefficient measurements with the effects of the heat fluxes, mass fluxes and vapor mass qualities. The transition boundaries among the three heat transfer regions are given.

(Some figures in this article are in colour only in the electronic version)

Nomenclature

A_c	Cross-sectional area of each triangular microchannel (m^2)
b	Side wall width of the triangular microchannel (m)
$\mathrm{Bo} = q/Gh_{fg}$	Boiling number
C_{pf}	Specific heat (J kg^{-1} K^{-1})
d	Hydraulic diameter of the microchannel (m)
G	Mass flux (kg m^{-2} s^{-1})
L_{sp}	Single-phase liquid flow length (m)
L_h	Total heating length (m)
h	Heat transfer coefficients (W m^{-2} K^{-1})
h_{fg}	Latent heat of evaporation (J kg^{-1})
h_{tp}	Two-phase heat transfer coefficients (W m^{-2} K^{-1})
I	Current passing through the thin film heater (A)
K_1	Momentum force due to evaporation relative to the inertia force
m	Mass flow rate (kg s^{-1})
N	Total number of parallel microchannels

p_{sat}	Saturated pressure of the fluid (bar)
q	Effective heat flux based on the side wall channel area (W m^{-2})
Q	Effective heating power (W)
Re	Liquid Reynolds number
T	Temperature (°C)
T_{in}	Inlet liquid temperature (°C)
$T_f(z)$	Liquid temperature along the flow direction (°C)
$T_w(z, y)$	Chip temperatures in z and y coordinates (°C)
U	Inlet liquid velocity (m s^{-1})
V	Voltage applied on the thin film (V)
W	Width of the heating film (m)
x	Thermodynamic vapor mass quality
y	Width direction coordinate (m)
z	Flow direction coordinate (m)

Greek symbols

Δp	Pressure drop (kPa)
$\Delta T_{sub,in} = T_{sat} - T_{in}$	Inlet liquid subcooling (°C)
ρ	Density (kg m^{-3})
ν	Kinematic viscosity (m^2 s^{-1})
μ	Viscosity (Pa s)
φ	The ratio of heat transfer to the working fluid to the total heating power

Subscripts

f	Liquid phase
g	Vapor phase
in	Inlet condition
out	Outlet condition
sat	Saturated condition
w	Chip wall

1. Introduction

Compared with microscale single-phase flow and heat transfer, microscale boiling heat transfer offers some advantages such as higher heat transfer coefficients and low mass flow rates. Microscale boiling heat transfer could have wide applications in fields such as high heat flux electronic chip cooling, ink-printer design and optical multiplexers.

Kandlikar [1] classified the channels in terms of the hydraulic diameter, d, as conventional channels for d greater than 3 mm, minichannels from 200 μm to 3 mm and microchannels from 10 to 200 μm, respectively. The range of hydraulic diameters below 200 μm is becoming important in many microelectromechanical systems (MEMS). Development of these micro systems in biomedical, genetic research has opened a new field for microscale boiling heat transfer. However, much smaller hydraulic diameter requires very high pumping power; thus the channel size may have optimal values, depending on the different applications.

Microscale boiling heat transfer needs a better understanding of the bubble dynamics such as bubble nucleation, growth, coalescence, flow patterns, pressure drops, heat transfer coefficients and critical heat fluxes. Therefore, the micro devices or systems can be operated safely in a controllable manner. Recent reviews on these topics can be found in Kandlikar [1, 3] and Thome [2].

Table 1 summarizes the related flow boiling heat transfer studies in miniature/micro scale channels, published in some recognized journals. The literature has become rich in recent years. However, general conclusions in this field are far from being drawn. Some conclusions may be conflicting, due to the difficulties in instrumentation. Early miniature/micro scale boiling heat transfer studies were performed using R-113, R-12, R-141b, R-124, R-134a, FC-82 and water as working fluids. The test sections were made of copper, aluminum, stainless steel capillary tubes or parallel channels [4–10, 12, 14–16]. These studies were mainly for refrigeration application purposes, with hydraulic diameters ranging from a couple of millimeters to several millimeters.

In macroscale boiling heat transfer, there are two major heat transfer mechanisms, nucleate boiling heat transfer dominant, forced convective heat transfer dominant or combined mechanism dominant heat transfers. The analysis in terms of the effects of heat fluxes and mass fluxes (sometimes including the vapor qualities) is also widely extended in the microscale. The heat flux dependent heat transfer coefficients result in nucleate boiling heat transfer being dominant [4, 5, 10]. Example studies showing the forced convective heat transfer dominant are [12, 16]. Others belong to the hybrid or some special heat transfer mechanisms [6, 7, 9, 11, 13, 15].

If the hydraulic diameter is decreased continuously, the wall superheating is increased before an active nucleate site is created. Once the bubble nucleation starts, the quick release of the energy into the vapor bubble causes rapid bubble growth and occupies the entire channel. The rapid bubble growth pushes the vapor/liquid interface traveling both downstream and upstream, and leads to reversed flow among the parallel microchannels [3]. Kandlikar [3] stated that the periodic bubble nucleation, growth, dry-out and liquid refilling processes are similar to those of nucleate boiling except that the whole microchannel acts as the heated wall surface. Nucleate boiling heat transfer always plays a major role while the convective heat transfer is suppressed over the entire vapor quality region [3].

Thome [2] summarized the miniature boiling heat transfer studies and concluded that the available experimental data mostly support the fact that the heat transfer coefficients are not a function of vapor quality nor of mass flux (in contrast to macrochannel trends), but a function of heat fluxes and saturation pressure. However, this conclusion has many exceptions that under some circumstances the microscale boiling heat transfer coefficients are affected by the mass fluxes and vapor qualities [6, 7, 9, 11–13, 15, 16]. Instead, Thome [17] proposed the transient evaporation of thin liquid films surrounding the elongated bubbles. It is noted that the proposed flow patterns include a succession of bubble slugs with protruding advancing vapor/liquid interface and flat receding interface, which are based on the air–water adiabatic two-phase flow in a 0.8 mm capillary tube.

Jiang *et al* [11], Hetsroni *et al* [18], Wu and Cheng [19] are authors who have performed microscale boiling heat

Table 1. Miniature/micro channel boiling heat transfer studies by different authors.

Author and year	Channel geometry and materials	Working fluid and parameter ranges	Remarks (focus on heat transfer performance)
Lazarek and Black (1982) [4]	Single tube, $d = 3.15$ mm	R-113, $G = 125$–750 kg m^{-2} s^{-1}, $q = 14$–380 kW m^{-2}, $P = 1.3$–4.1 bar	Nucleate boiling dominant, $h_{tp} = f(q)$ but independent of x, G
Wambsganss *et al* (1993) [5]	Single stainless steel tube, $d = 2.92$ mm	R-113, $G = 50$–300 kg m^{-2} s^{-1}, $x = 0$–0.9, $q = 8.8$–90.75 kW m^{-2}, $P_{out} = 1.24$–1.6 bar	Nucleate boiling dominant, $h_{tp} = f(q)$ but independent of x and G
Tran *et al* (1996) [6]	Single brass tube, $d = 2.46$ mm; Single brass rectangular channel, $d = 2.40$ mm (4.06×1.70 mm^2)	R-12, $G = 44$–832 kg m^{-2} s^{-1}, $x = 0$–0.94, $q = 3.6$–129 kW m^{-2}, $P = 5.1$, 8.2 bar,	Nucleate boiling dominant (wall superheat above 2.75 °C), convective boiling dominant (wall superheat blow 2.75 °C)
Kew and Cornwell (1997) [7]	Single stainless steel tubes, $d = 1.39$–3.69 mm	R-141b, $G = 188$–1480 kg m^{-2} s^{-1}, $q = 9.7$–90 kW m^{-2}	Four mechanisms: nucleate boiling, confined bubble boiling, convective boiling and partial dry-out
Ravigururajan (1998) [8]	54 parallel rectangular channels, $d = 0.850$ mm (0.27×1.00 mm^2)	R-124, $V = 75$–250 ml min^{-1}, $q = 20$–700 kW m^{-2}, $x = 0$–0.5	h_{tp} decreases with vapor quality and wall superheat
Yan and Lin (1998) [9]	28 parallel tubes, $d = 2$ mm	R-134a, $G = 50$–200 kg m^{-2} s^{-1}, $q = 5.0$–20 kW m^{-2}	$h_{tp} = f(q, x, T_{sat})$
Bao *et al* (2000) [10]	Single copper tube, $d = 1.95$ mm	R-12, HCFC 123, $G = 50$–1800 kg m^{-2} s^{-1}, $q = 5$–200 kW m^{-2}, $P = 2$–5 bar, $x = 0$–0.9	Nucleate boiling dominant, $h_{tp} = f(q)$ but independent of x and G
Jiang *et al* (2001) [11]	35 parallel silicon triangular channels, $d = 0.026$ mm	Water, $V = 2$ ml min^{-1}, $Q = 5.1$–29.9 W	Local nucleate boiling (low input power range), unstable slug flow as upstream bubbles (intermediate input power), stable annular flow (high input power)
Lee and Lee (2001) [12]	Single stainless steel rectangular channels, $d = 1.569$–7.273 mm (20 mm wide, 0.4–2 mm deep)	R-113, $G = 50$–200 kg m^{-2} s^{-1}, $q = 0$–15 kW m^{-2}, $x = 0.15$–0.75	Forced convective boiling dominant, $h_{tp} = f(G, x)$ but almost independent of q
Hetsroni *et al* (2002) [13]	21 parallel silicon triangular channels, $d = 0.130$ mm	Vertrel XF, $G = 148$–290 kg m^{-2} s^{-1}, $q = 22.6$–36 kW m^{-2}	$h_{tp} = f(q, x, G)$
Warrier *et al* (2002) [14]	5 parallel aluminum rectangular channels, $d = 0.75$ mm	FC-84, $G = 557$–1600 kg m^{-2} s^{-1}, $q = 0$–59.9 kW m^{-2}, $T_{in} = 26$, 40, 60 °C	h_{tp} decreases with increasing x
Yu *et al* (2002) [15]	Single tube, $d = 2.98$ mm	Water, $G = 50$–200 kg m^{-2} s^{-1}, $q = 50$–200 kW m^{-2}, T_{in} = ambient to 80 °C	Nucleate boiling dominant (wall superheat above 8 °C), transition boiling dominant (wall superheat blow 8 °C)
Qu and Mudawar (2003) [16]	21 parallel copper rectangular channels, $d = 0.349$ mm (0.231×0.713 mm^2)	Water, $G = 135$–402 kg m^{-2} s^{-1}, $q = 10$–1300 kW m^{-2}	Forced convective boiling dominant, h_{tp} decreases with increasing x
Kandlikar (2004) [3]	Not mentioned	Not mentioned	Nucleate boiling dominant, rapid bubble growth and flow reversal
Thome *et al* (2004) [17]	Theoretical	Theoretical	A three-zone flow boiling model including bubble frequency, minimum liquid film thickness at dry-out and liquid formation thickness

transfer experiments in silicon microchannels. Jiang *et al* [11] carried out the microscale boiling heat transfer for hydraulic diameters of 26 and 53 μm. Fewer nucleation sites were observed at low heating powers. At moderate heating powers, unstable slug flow was observed to pass through the channels, suppressing the active nucleation sites. Higher heating power results in stable annular flow with a clear vapor/liquid interface without liquid droplets in the vapor core. Hetsroni *et al* [18] performed high speed flow visualization of the microscale boiling heat transfer in three silicon microchannel heat sinks. The low heat flux regime results in the presence of a liquid phase in part of the microchannels. The high heat flux regime is characterized by convective boiling, in all parallel microchannels, accompanied by the quasi-periodic dry-out and refilling of the microchannels. Wu and Cheng [19] performed two-phase flow instability experiments in silicon microchannels. The pressures and fluid/wall temperatures are found to be oscillating with large amplitude/long period with

the cycle period in the range of 10–100 s if the pressure drop across the microchannel test section is out of phase with the mass fluxes.

In our previous paper [20], we found that all microchannels repeat the transient flow patterns on a timescale of milliseconds, while the fluid pressures/temperatures are stable. A full cycle includes three substages: liquid refilling stage, bubble nucleation, growth and coalescence stage and transient annular flow stage. Paired or triplet bubbles are found to be nucleated and grow simultaneously in or very close to the channel corners at the same cross section. Once the paired or triplet bubbles coalesce, the quick release of the superheated liquid energy causes the bubble explosion phenomenon, separating the liquid slug into two parts and pushing the fluid out of the channels in less than 1 ms. In the transient flow stage, the liquid film that is drawn into the channel corners becomes less and less until a partial or even fully dried-out state is reached. Following this, the microchannels are ready to be refilled by the fresh incoming liquid.

The present paper is the extended work of our previous paper [20]. The microscale boiling heat transfer coefficients were obtained for 102 runs at different heat fluxes, mass fluxes and vapor mass qualities. It is found that the heat transfer characteristics can be subdivided into three regions by dividing the boiling numbers into three small ranges. Low boiling numbers result in increased heat transfer coefficients along the flow direction, medium boiling numbers yield the perfect nuclear boiling performance while high boiling numbers give convective heat transfer performance. Most importantly, we provide the link between the transient flow patterns and the measured heat transfer coefficients. There are two major reasons to perform such link, which are described as follows:

- Because the transient flow patterns are repeated periodically and a full cycle has three substages, each substage has different flow patterns leading to different heat transfer mechanisms. Linking the transient flow patterns and the measured heat transfer coefficients is useful to identify which heat transfer mechanism is the dominant.
- A lot of parameters affect the flow patterns and the heat transfer performances. Linking between them yields the major parameter governing the complex boiling phenomenon in microscale.

2. Experiment description

2.1. Silicon microchannels

Figure 1(*a*) shows the parallel silicon microchannel heat sink. The overall size of the silicon chip is 300 mm in length, 7 mm in width and 530 μm thick. Ten triangular microchannels were etched and centrally located in the silicon substrate, each 300 μm wide, 212 μm deep, forming a hydraulic diameter of 155.4 μm. The pitch distance between two neighboring microchannels is 150 μm. The overall size of the ten microchannels is 21.45 mm in length and 4.350 mm in width. A pyrex glass cover with the thickness of 410 μm was bonded with the silicon wafer; thus the high speed flow visualization could be performed. On the back side of the silicon wafer, a thin platinum film was deposited and driven by an ac power supply, providing a uniform heat flux. The thin platinum film has the same length as the silicon microchannels, 21.450 mm. For the chip safe operation purpose, the width of the heating film is 4.200 mm, which is narrower by half a triangular microchannel width. The effective heating length of the thin film is selected as 16.000 mm, forming an effective heating area of 16.000×4.200 mm^2. Such an area is also the optical view field for the infrared radiator image temperature measurements. Because the thin film has 'bright color', giving poor temperature readings for the IR image system, a very thin 'black lacquer' was painted on the surface of the thin heating film. A two-dimensional y–z coordinate was attached to the effective heating area, with z being the axial flow direction and y being the perpendicular width direction, as shown in figure 1(*b*). Also shown in figure 1(*b*) are the relative positions of the flow view field, the parallel microchannel area, the thin film heating area and the whole silicon wafer.

The silicon microchannels are fabricated using $\langle 1\,0\,0 \rangle$ double polished wafers, of size 4 inch. The wafers are cleaned. The following procedures were applied, as shown in figure 2 for the longitudinal view: (figure 2(*a*)) double side thermal oxidation layer deposited on the wafer to 3000 Å, (figure 2(*b*)) double side silicon nitride layers deposited to 1500 Å by low pressure chemical vapor deposition (LPCVD), (figure 2(*c*)) a standard photoresist layer spun on the wafer and baked as conventional and lithographic processing technique applied, (figure 2(*d*)) selective reactive ion etching (RIE) of the silicon nitride by 1500 Å, (figure 2(*e*)) selective RIE of the oxide layer to 3000 Å, (figure 2(*f*)) top side photoresist removal, (figure 2(*g*)) wet etching of the microchannel to the depth of 212 μm by KOH, (figure 2(*h*)) back side selective RIE of the silicon nitride and oxide, back side photoresist removal, (figure 2(*i*)) top side silicon nitride and oxide removal by RIE, (figure 2(*j*)) wafer bounded with the 7740 pyrex glass cover, (figure 2(*k*)) back side photoresist and lithographic procedure applied, (figure 2(*l*)) back side titanium layer deposited to 1000 Å; (figure 2(*m*)) back side Pt film deposition to 1000 Å.

2.2. Experimental set-up

As shown in figure 3(*a*), liquid acetone is pressurized by nitrogen gas and flows successively through a liquid valve, a 2 μm filter, the silicon wafer test section, a heat exchanger and finally returns to a liquid container. The high precision pressure regulator valve located between the nitrogen gas tank and the acetone tank was used to control the inlet pressure of the silicon microchannel heat sink. The temperature of the liquid tank is maintained by a constant temperature control unit (PID) with the uncertainty of ± 0.5 °C. The inlet liquid temperature of the silicon microchannel wafer can be kept by wrapping high quality heat insulation material on the outer surface of the connection tube between the outlet of the acetone tank and the inlet of the microchannel test section. The

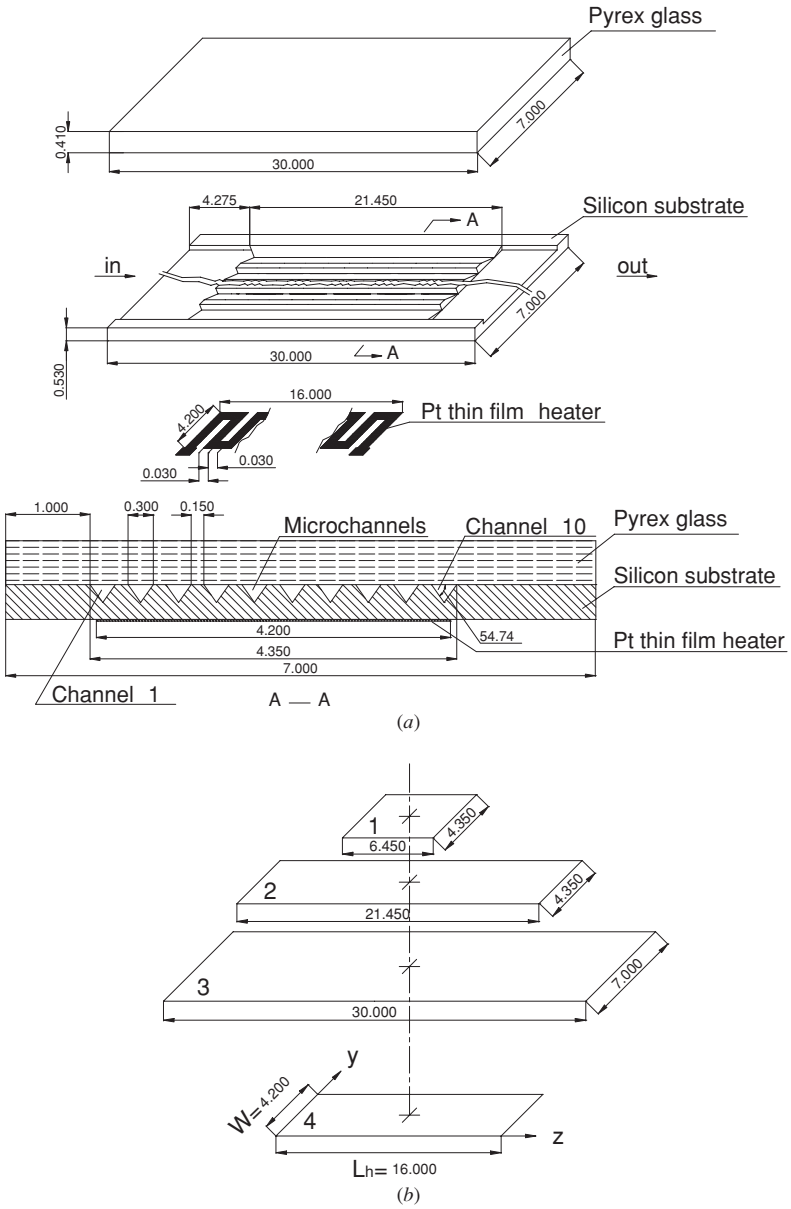

Figure 1. Silicon microchannel test section. 1: Flow view field; 2: microchannel area; 3: whole silicon chip; 4: effective thin film heater (all dimensions are in millimeters).

liquid mass flow rate was decided in terms of the increased liquid mass over a long period of time with a high precision electronic balance which has the measurement uncertainty of 0.02 g. The inlet/outlet fluid temperatures were measured by the high precision jacket thermocouples with a diameter of 1.0 mm and with an uncertainty of 0.2 °C. The inlet fluid pressure was measured by a Setra pressure transducer (Model 206), which was calibrated against a known standard and the uncertainty in the pressure measurements was less than 1%. A Senex differential pressure transducer was connected over the microchannel test section to obtain the pressure drop, with the uncertainty of 0.1%. All of the pressure and temperature signals were collected by a HP data acquisition system. Figure 3(*b*) shows a picture of our microfluidic optical system.

2.3. Chip temperature measurement

The wafer temperatures of the back side thin film were measured by a high resolution, high accuracy infrared radiator imaging system (FLIR ThermaCAM SC3000 IR). This system has a thermal sensitivity of 0.02 °C at 30 °C, a spatial resolution of 1.1 mrad, a typical resolution of 320 × 240 pixels over the focused area, allowing the precise determination of the maximum temperature and temperature gradients over the whole heating area.

The IR camera was centrally located so that the heating area of the silicon wafer (16.000 × 4.200 mm^2) is in the view field. The IR imaging system was connected to a PC. The PC stores the image file and the corresponding data file which contains 6080 data points related to the focused thin film heating area.

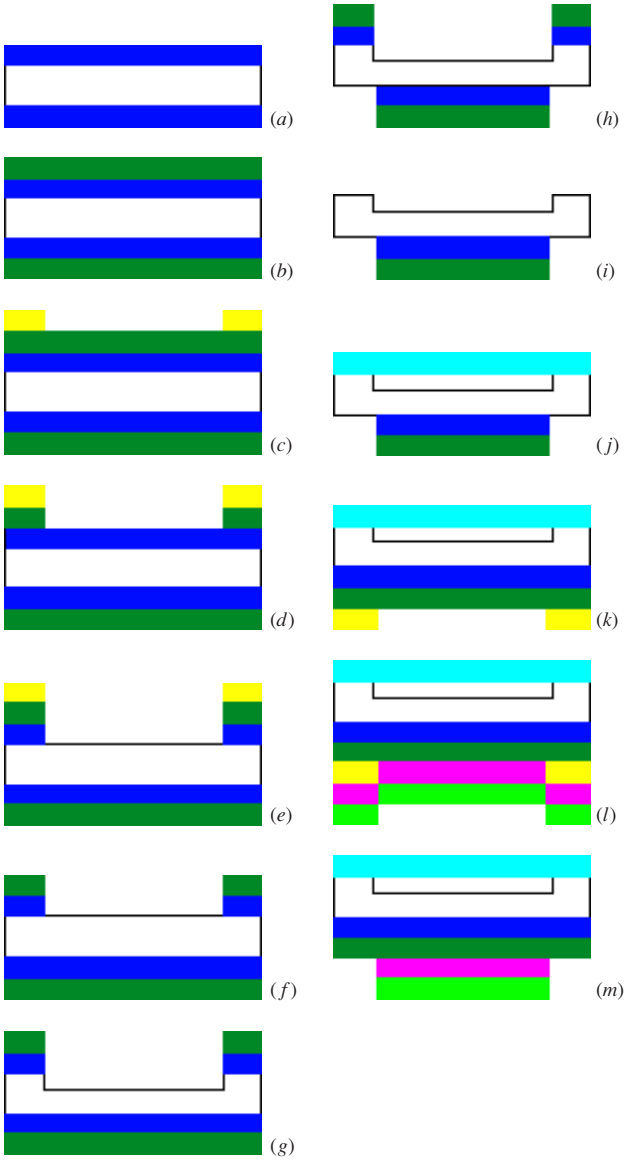

Figure 2. MEMS fabrication (silicon: , silicon nitride: , photosensitive resist: , glass: , silicon oxide: , titanium: platinum:).

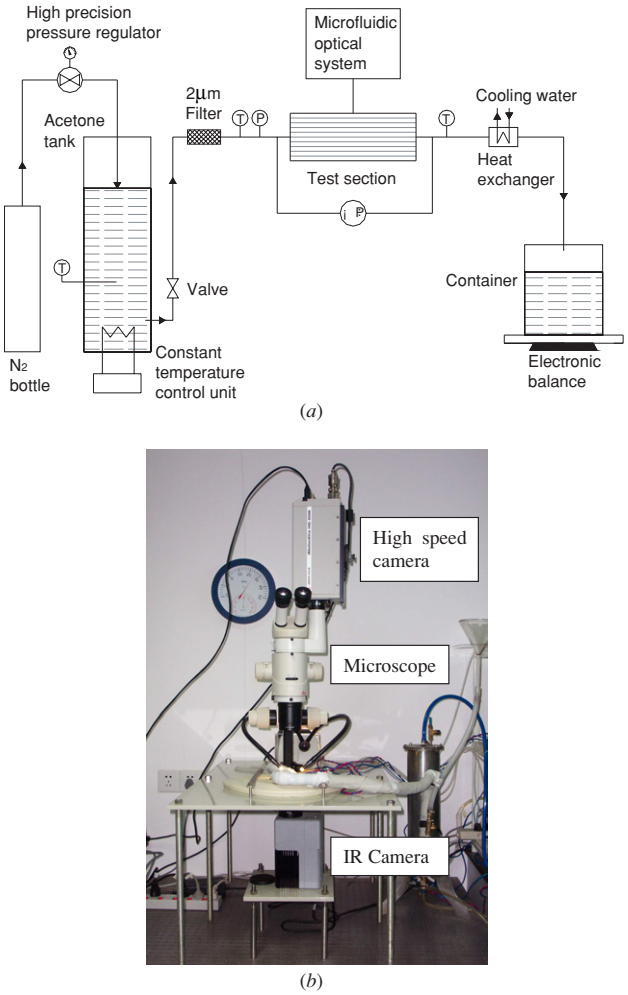

Figure 3. (*a*) Experimental system. (*b*) Microfluidic optical system.

The IR temperature measurement requires a careful calibration of the emissivity, which depends strongly on the surface topography and the wavelengths that are interrogated [21]. A very thin 'black lacquer' was uniformly painted on the thin film surface of the silicon wafer. An emissivity of approximately 0.94 yields good measurement accuracies. The temperature dependence of emissivity within the present experimental range can be neglected. Using this technique, the IR imaging system was calibrated against a set of known standard temperatures with an accuracy of 0.4 °C. The IR image system offers advantages for the chip temperature measurements over the conventional method using thermocouples. Attaching the thermocouple wires on the chip surface disturbs the temperature field and the number of measurement locations is quite limited. The combined optical system consists of a Leica M stereo-microscope (Germany) and a HG-100K high speed camera (see figure 3(*b*)). Such a system is described in Xu *et al* [20]. For such an optical system, the white image represents the liquid phase while the black image shows the vapor phase.

2.4. Data reduction

The liquid used in the present study is pure liquid acetone (CH_3COCH_3, molecular weight 58.08, purity >99.5%). Acetone has lower saturated temperature at atmospheric pressure and is widely used as the working fluid in micro heat pipes and loop heat pipes. Other working fluids, such as methanol, ethanol, FC-72, can also be used for the microscale boiling heat transfer experiments [22]. They have similar thermal physical properties. Water is a different coolant in its higher saturated temperature and larger surface tension and latent heat of evaporation. Because the wall surface of the silicon microchannels is very smooth, water needs very high chip temperatures to create the onset of boiling (ONB). Thus, water is not used in the present study.

The physical properties of acetone are taken from [23]. Some of the important properties are described in [20]. Before performing the data reduction process, it is necessary to define the mass flux G, heat flux q and liquid Reynolds number Re.

The mass flux G is defined as the total mass flow rate over the ten cross section areas of the triangular microchannels, $G = m/(NA_C)$, where m is the mass flow rate (kg s^{-1}), N is the total number of microchannels, A_C is the cross-sectional area of a single triangular microchannel (m^2). The mass flow rate m is computed as the increased mass over a given period of time.

The heat flux is defined as $q = \varphi VI/(2NbL_h)$, where V and I are the voltage and current applied to the thin film heater, b and L_h are the side wall width and the effective length of the heating film. φ is the ratio of the heat received by the fluid to the total heating power, which is described in section 2.5.

The liquid Reynolds number is defined as $\mathrm{Re} = Ud/\nu$, where U is the average flow velocity assuming the total fluid is flowing as the liquid phase only, d is the hydraulic diameter of the triangular microchannels and ν is the liquid kinematic viscosity based on the inlet liquid temperature.

The two-dimensional heat transfer coefficients were provided corresponding to the flow direction (z-coordinate) and the width direction (y-coordinate). Because the inlet liquid has some certain degree of subcooling, the whole effective heating area is divided into two areas, the single-phase liquid flow area and the two-phase flow area. The length of the subcooled liquid area could be decided in terms of the energy conservation equation as

$$L_{\mathrm{sp}} = mC_{\mathrm{pf}}L_h(T_{\mathrm{sat}} - T_{\mathrm{in}})/Q \tag{1}$$

where Q is the effective heating power. In the liquid flow area, a linear liquid temperature distribution along the flow direction is assumed. The liquid temperature ($T_f(z)$), the local vapor mass quality ($x(z)$) and the heat transfer coefficient ($h(z, y)$) were computed as

$$T_f(z) = T_{\mathrm{in}} + z(T_{\mathrm{sat}} - T_{\mathrm{in}})/L_{\mathrm{sp}} \tag{2}$$

$$x(z) = \frac{C_{\mathrm{pf}}(T_{\mathrm{in}} - T_{\mathrm{sat}}) + zQ/mL_h}{h_{fg}} \tag{3}$$

$$h(z, y) = \frac{q}{T_w(z, y) - T_f(z)} \tag{4}$$

$T_w(z, y)$ is the local chip temperature. It is noted that $x(z)$ is negative and the liquid temperature is computed based on equation (2) in the single-phase liquid area. In the two-phase area, $x(z)$ is positive and the fluid temperature $T_f(z)$ uses the saturation temperature T_{sat} relating to its pressure.

2.5. Uncertainty analysis

The uncertainties of the direct measurement parameters are: the microchannel upstream pressures 1%, the pressure drops across the silicon wafer 0.1%, the inlet/outlet fluid temperatures 0.2 °C, and the chip temperature measurements using the IR image system 0.4 °C. These parameters have higher accuracies. Other parameters, such as the mass flux G, heat flux q and the liquid Reynold numbers Re, are deduced in subsection 2.4. Performing the standard error analysis yields uncertainties of the mass flux of 2.1% and of the liquid Reynolds numbers of 2.96%. A lot of factors affect the effective heating power. The heat loss of the microchannel test section includes the components of radiation and natural convection heat transfer from the heated chip wall surface to the environment. The heat loss also includes the heat conduction from the silicon wafer to its upstream and downstream connection tubes. It is quite difficult to estimate the heat flux uncertainties accurately. However, a set of single-phase heat transfer experiments were performed before the boiling heat transfer tests started. The thermal efficiencies, φ, could be decided with the net heat received by the acetone coolant (computed from the mass flow rate and the inlet/outlet fluid temperature difference) divided by the total applied heat input. It is found that three operation parameters: the heat inputs (the powermeter readings), the inlet liquid temperatures and the mass flow rates affect the thermal efficiencies. Among them the heat input is the major factor. Generally the higher the heat input is, the greater the thermal efficiency is. The experimentally decided thermal efficiencies are plotted versus the heat input in figure 4. It is noted that the heat inputs have similar ranges for both the single-phase and boiling two-phase heat transfer experiments. Seen from figure 4 the lowest thermal efficiency is 0.77 and the largest value 0.90. The mean thermal efficiency of 0.84 is used to deduce the effective heating power that is used for the boiling heat transfer experiments.

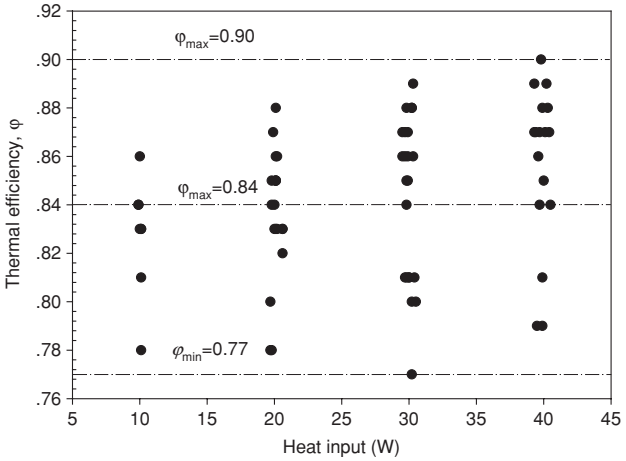

Figure 4. Experimentally decided thermal efficiency for the present study.

3. Transient flow pattern based heat transfer analysis

3.1. Description of the transient flow patterns

Because the cycle period is much shorter than the response times of the fluid pressure and temperature sensors, these sensors give a stable signal output. It is noted that some flow instabilities such as Ledinegg flow instability may take place in two-phase flow and heat transfer loops under some circumstances. These flow instabilities show large oscillation amplitudes and long cycle periods. However, increasing the pressure drops upstream of the boiling test sections is useful to stabilize the test loop. For the present study, the 2 μm filter located upstream of the silicon wafer provides a larger upstream pressure drop, the test loop is stable. Figures 5 and 6 illustrate the transient flow patterns for the medium and higher boiling number runs, corresponding to medium and higher outlet vapor qualities, respectively. In both runs a full cycle can be subdivided into three substages.

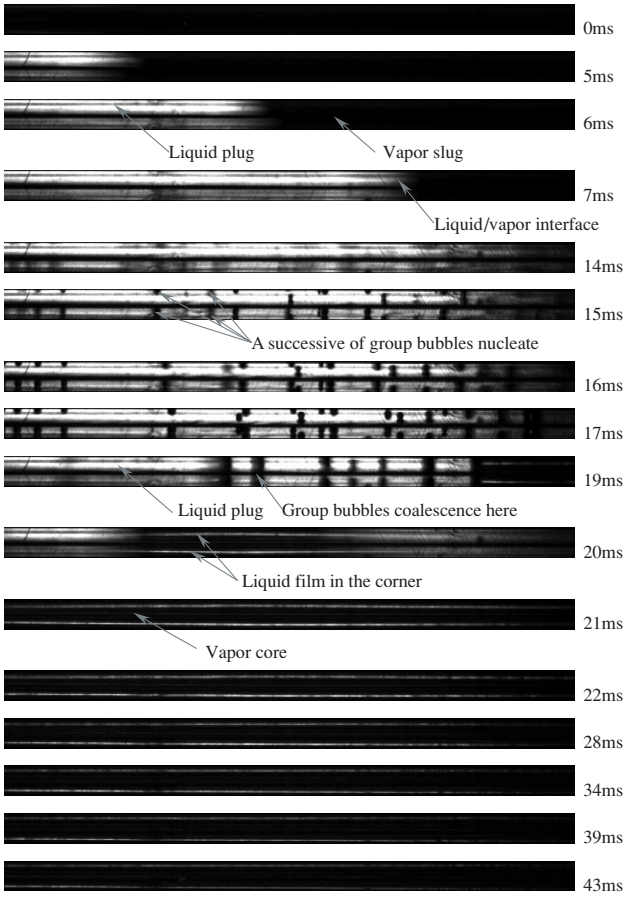

Figure 5. Transient flow patterns for medium boiling number ($T_{in} = 30.8$ °C, $\Delta p = 30.41$ kPa, $G = 110.1$ kg m^{-2} s^{-1}, $q = 141.9$ kW m^{-2}, $x_{out} = 0.5268$, Re $= 65.2$, cycle period $= 43$ ms, channel 9).

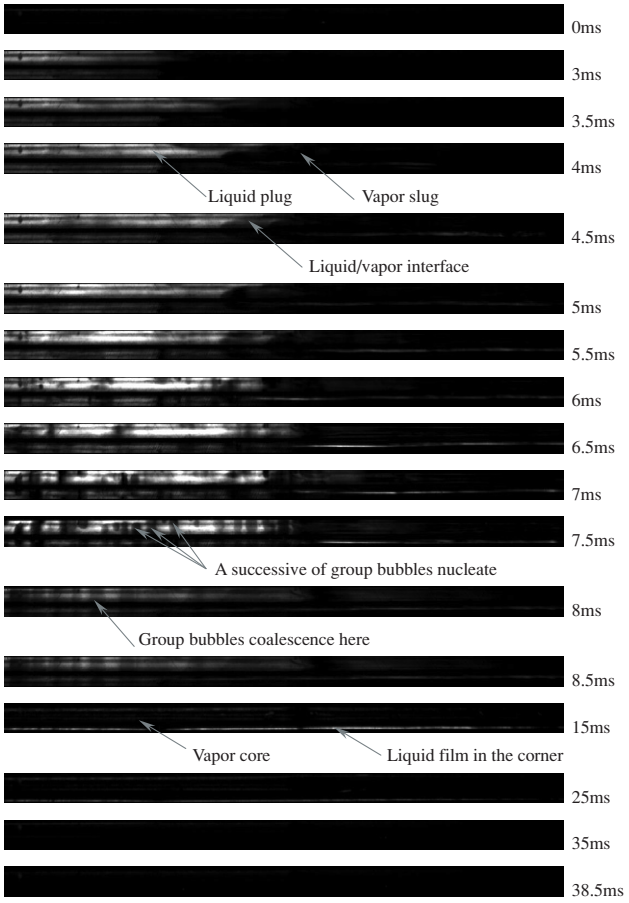

Figure 6. Transient flow patterns at high boiling number ($T_{in} = 24.7$ °C, $\Delta p = 30.84$ kPa, $G = 64.8$ kg m^{-2} s^{-1}, $q = 166.0$ kW m^{-2}, $x_{out} = 1.1496$, Re $= 37.7$, cycle period $= 38.5$ ms, channel 10).

3.1.1. Liquid refilling stage. A typical full cycle can be defined from the end of the previous cycle when all of the microchannels are full of high quality vapor or even in the dried-out condition (see $t = 0$ ms in figure 5). Suddenly a liquid plug enters the microchannel, separating the whole microchannel into two parts, the single-phase liquid plug and the vapor slug (see $t = 5$–14 ms in figure 5). The vapor/liquid interface is sometimes flat. The liquid plug may or may not entrain the inverse bubble slug as defined in [20].

3.1.2. Bubble nucleation, growth and coalescence stage. Once the entered liquid plug is heated up to a certain degree of superheating (such liquid superheating is estimated to be 2 °C for water flowing in a 200 μm microchannel [3]), paired or triplet group bubbles are nucleated simultaneously in or very close to the channel corners at the same cross section (see $t =$ 15 ms in figure 5). This may be attributed to the following reasons: (1) the two side channel corners at the same cross section always have the same liquid temperatures and flow velocities, which may be different from the mean values at such cross section. The lower base channel corner may have slightly higher temperature than the side corners. However, such temperature difference is quite small due to the very high silicon thermal conductivity. (2) Each microchannel has three similar corner angles. The two side corners of the triangular microchannels have the base angles of 54.74°, while the bottom corner has the angle of 70.52°, using the standard MEMS fabrication method. Group bubbles evolve following their nucleation (see $t = 16$–18 ms in figure 5).

Once the paired or triplet bubbles coalesce with each other and occupy the whole cross section of the microchannel, the enhanced heat transfer from the superheated liquid to the vapor/liquid interface induces a sharp increase of the vapor pressure. The explosive bubble coalescence at the same cross section quickly pushes the fluid out of the microchannel (see $t = 20$ ms in figure 5).

From bubble nucleation to bubble coalescence, the time period is only 4 ms for figure 5. In this process, the fluid inside the microchannel is temporarily in a stationary state.

3.1.3. Transient liquid film evaporation stage. The coalesced bubble quickly pushes the fluid out of the microchannels downstream and upstream, leaving a liquid film attached to the microchannel wall surface. The liquid film has the greatest possibility of being accumulated in the triangular channel corners. Then the transient liquid film evaporation stage starts. The liquid film becomes thinner and thinner with time (the two white lines gradually becoming dimmer and dimmer), until high quality vapor or even a dried-out condition is reached and

the new liquid refills the microchannels (see $t = 20$–43 ms in figure 5).

Figure 6 shows the transient flow patterns for the high boiling number run. The flow patterns show a similar phenomenon to that of figure 5. However, the major differences are: bubbles can be nucleated anywhere for the time statistical point of view at medium boiling number, but they shift to the channel upstream at high boiling numbers. The transient annular flow stage lasts much longer for the higher boiling numbers. The above differences strongly affect the dominant heat transfer mechanisms for the medium and high boiling numbers. It is noted here that figure 6 in this paper shows the same phenomenon as that of figure 14 in [20], but they are not identical because they are taken from different channels and different cycles.

3.2. Transient flow pattern based heat transfer mechanism

Microscale boiling heat transfer is indeed a complicated phenomenon. Corresponding to the above transient flow patterns on the timescale of milliseconds, there are the following heat transfer mechanisms:

3.2.1. Single-phase liquid forced convective heat transfer. Single-phase liquid forced convective heat transfer takes place in the liquid refilling stage. Because the mean liquid Reynolds number is quite small, such as 65.2 for figure 5 and 37.7 for figure 6, at such low liquid Reynolds number, the single-phase liquid forced convective heat transfer could not be significant.

3.2.2. Nucleate boiling heat transfer. Nucleate boiling heat transfer occurs when the new paired or triplet bubbles are nucleated simultaneously in the same cross section of the microchannels, including the growth and coalescence processes. Generally the liquid in microchannels requires higher superheating to be nucleated; once the nucleation sites are initiated, the quick release of the energy to the vapor phase results in very high bubble growth and coalescence rates, leading to the bubble explosion phenomenon. The nucleate heat transfer may be important from the time averaging point of view.

3.2.3. Vapor explosive induced forced convective heat transfer. The bubble explosion causes very high velocities of the separated fluids traveling upstream and downstream. The vapor explosive induced velocity can be several times the normal liquid refilling velocity. Even though the mean liquid Reynolds number is small, vapor explosive induced forced convective heat transfer could not be neglected, and may be important under some circumstances. The previous articles stated that the flow in microchannels is always laminar. However, the vapor explosive induced velocity can be very high and the flow may be instantaneously switched to turbulent once the bubble coalescence is triggered. We used a recording rate of a couple of thousand frames per second and the fluid can be out of the flow view field in 0.5 or 1.0 ms after the bubble coalescence. Further study of the bubble explosion phenomenon is suggested, using an ultra high speed camera system.

3.2.4. Transient liquid film evaporation heat transfer. Transient liquid film evaporation heat transfer takes place in the liquid refilling stage, in which part of the microchannels is flushed by the inlet fresh liquid while the remaining part is still covered by the vapor slug. It also takes place at the last substage at which the entire microchannel length is covered by the annular flow, with the liquid film thickness becoming less and less with time.

3.2.5. Saturated or slightly superheated vapor heat transfer. The microchannel may partially or fully dry out at the end of each cycle. Slightly superheated vapor heat transfer may also be possible for the run with mean outlet vapor quality slightly larger than unity.

3.3. Time and spatial statistical characteristics of boiling heat transfer in parallel microchannels

Because the transient flow patterns at high heat fluxes evolve so fast, the thermal inertia of the silicon material flattens the chip temperatures versus time. Thus, the chip temperatures measured by the IR image system actually reflect the time averaged values. However, the spatial chip temperature distributions can still be detected due to the uneven liquid and vapor phases periodically flushing the microchannels.

The four flow patterns defined in [20] also satisfy the statistical principle, the probabilities of the flow pattern A: liquid plug/vapor slug is smallest (this flow pattern is in the liquid refilling stage), while the annular flow is the largest.

It is interesting to note that only some of the microchannels are refilled by the fresh liquid in a full cycle. However, if a specific microchannel is not refilled by the liquid in the current cycle, it may be refilled in the next cycle. The liquid refilling probabilities also satisfy the statistical principle, with the center channels slightly higher and the side channels slightly lower. For the parallel microchannels, the inlet/outlet reservoirs balance the pressures among the microchannels. The statistical principle of the liquid refilling probabilities is attributed to the parallel microchannel effects.

3.4. Effect of the boiling number on microscale boiling heat transfer

The boiling number is the non-dimensional heat flux, coupling with the mass flux and the latent heat of evaporation. It has an internal relationship with the single-phase liquid flow length, and the outlet equilibrium thermodynamic quality. Rewriting equation (1), we obtain the ratio of the single-phase liquid flow length to the whole heated microchannel length as

$$\frac{L_{\mathrm{sp}}}{L_h} = \frac{1}{\mathrm{Bo}} \times \frac{A_c}{2bL_h} \times \frac{C_{pf}\Delta T_{\mathrm{sub,in}}}{h_{fg}} \tag{5}$$

where A_c is the cross sectional area of each microchannel, $\Delta T_{\mathrm{sub,in}} = T_{\mathrm{sat}} - T_{\mathrm{in}}$ is the inlet liquid subcooling. On the right-hand side of equation (5), $A_c/2bL_h$ reflects the cross sectional area relative to the side wall heated surface area, $C_{pf}\Delta T_{\mathrm{sub,in}}/h_{fg}$ is the non-dimensional inlet liquid subcooling.

The outlet equilibrium vapor mass quality in equation (3) can also be rearranged as

$$x_{\text{out}} = \text{Bo} \times \frac{2bL_h}{A_c} - \frac{C_{pf}\Delta T_{\text{sub,in}}}{h_{fg}}. \quad (6)$$

It is seen from equations (5), (6) that the boiling number is directly related to L_{sp}/L_h and x_{out}. The smaller the Bo number is, the longer L_{sp} and lower x_{out} is. Inversely, higher Bo number causes shorter L_{sp} and higher x_{out}. The boiling number is widely used in the boiling heat transfer analysis and correlations, both on macro and micro scales. Later in this section we will show that L_{sp}/L_h and x_{out} related to the boiling number strongly affect the heat transfer coefficient distributions along the flow direction (or the local vapor qualities).

Kandlikar [3] proposed the important parameter, the K_1 number, representing the momentum force due to evaporation relative to the inertia force, as

$$K_1 = \left(\frac{q}{Gh_{fg}}\right)^2 \frac{\rho_f}{\rho_g} = \text{Bo}^2 \frac{\rho_f}{\rho_g} \quad (7)$$

where K_1 consists of the square of the boiling number and the liquid to vapor density ratio. The K_1 number is important to characterize the microscale boiling heat transfer when different working fluids are considered. For the present study, only the one working fluid acetone is used, thus the boiling number is enough for the heat transfer analysis.

For a specific working fluid, the present experimental results show that the boiling number, not the heat flux only, governs the heat transfer. The boiling number provides information on the bubble nucleation locations (or the spatial bubble nucleation site probabilities), and the force balance between the evaporation momentum force relative to the inertia force. Let us divide the boiling number into low, medium and high regions and link the transient flow patterns with the heat transfer mechanisms.

3.4.1. Heat transfer at low boiling number. At lower boiling number, the length of the single-phase liquid flow covers a larger percentage relative to the whole heating length. The bubble nucleation sites have the largest possibilities of taking place close to the end of the heating length. The heat transfer is enhanced in the bubble nucleation areas. Dry-out may not occur even at the end of the heating area. Therefore along the flow direction, the heat transfer coefficients should be increased by increasing the local vapor mass quality, x, in the two-phase area. The transient flow patterns are not available due to the bubble nucleation sites being mostly downstream of the optical view field of the high speed camera.

3.4.2. Heat transfer at medium boiling number. Figure 5 illustrates the transient flow patterns for a full cycle at medium Bo. It is noted that bubble nucleation sites can take place anywhere along the flow direction (such bubble nucleation sites may have larger probabilities of taking place in the microchannel central area in the axial flow direction under some conditions). Nucleate boiling heat transfer contributes the major part. The forced convective heat transfer in the transient annular flow stage and induced by the bubble explosion phenomenon is small. The microscale boiling heat transfer in a cycle is similar to a successive process of bubble nucleation, growth (the growing bubble is expelling the liquid out of the cavity), and departure from the cavity followed by the refilling of fresh liquid, inside a cavity. Due to the nucleate boiling heat transfer being dominant, heat transfer being coefficients are strongly dependent on the heat flux, but not influenced by the mass flux and vapor mass quality variations.

3.4.3. Heat transfer at high boiling number. Figure 6 shows the transient flow patterns for the high boiling number run. The bubble nucleation sites shift to the microchannel upstream, qualitatively consistent with the short single-phase liquid flow length given by equation (5). For most time of the cycle period, the microchannel is covered by the annular flow (a liquid film may exist between the vapor core and the channel wall; the channel corners have the largest possibilities of accumulating a liquid film due to the surface tension force effect). The cycle period is becoming shorter. The strong explosive bubble coalescence results in high evaporation momentum force, pushing the fluid out of the microchannel very quickly for each cycle. The bubble explosive induced forced convective heat transfer plays the major role. Thus we deduce that the heat transfer coefficients are mainly dependent on the mass flux, and less on the heat flux. On the other hand, the partial or fully dried-out probabilities are increased along the flow direction. This effect results in decreased heat transfer coefficients along the flow length (or the local vapor qualities).

The transient flow pattern based heat transfer analysis in the three boiling number regions is consistent with the measured heat transfer coefficients, which are described in the following section.

4. Microscale boiling heat transfer measurements

4.1. Experiment runs and the transition boundaries

In total we performed boiling heat transfer experiments for 102 runs over broad parameter ranges: inlet pressures of 1–2 bar, pressure drops of 10–100 kPa, inlet temperatures of 24–45 °C, mass fluxes of 64–600 kg m^{-2} s^{-1}, heat fluxes of 150–480 kW m^{-2}. The x_{out} and the Bo have ranges of 0.07–1.15 and 0.69×10^{-3}–5.046×10^{-3}, respectively. Table 2 summarises the 102 runs, in which x_{out} and Bo are clearly marked. The last column shows the heat transfer region to which the corresponding run belongs. The three heat transfer regions are identified as regions 1, 2 and 3, which correspond to low, medium and high boiling numbers, with the ranges of 0.69×10^{-3}–1.184×10^{-3}, 1.574×10^{-3}–3.219×10^{-3} and 3.562×10^{-3}–5.046×10^{-3}, respectively. The transition regions are identified as $1 \rightleftarrows 2$ and $2 \rightleftarrows 3$.

Figure 7(a) shows the heat transfer performances in the three regions. Negative x represents the single-phase liquid flow area based on the thermodynamic equilibrium. Beyond $x = 0$ is the two-phase flow area, in which heat transfer coefficients increase along the flow direction for low boiling number (region 1), are nearly constant versus x for medium boiling number (region 2) and decrease along the flow direction for high boiling number (region 3). The transition boundaries among the three heat transfer regions are

Table 2. The present microscale boiling heat transfer test runs.

Run	p_{sat} (bar)	T_{in} (°C)	G (kg m^{-2} s^{-1})	q (kW m^{-2})	x_{out}	Bo $\times 10^3$	$K_1 \times 10^3$	Region	Run	p_{sat} (bar)	T_{in} (°C)	G (kg m^{-2} s^{-1})	q (kW m^{-2})	x_{out}	Bo $\times 10^3$	$K_1 \times 10^3$	Region
1	1.17	24.6	64.8	166.0	1.13	5.046	8.292	3	27	1.29	34.9	243.3	481.1	0.87	3.936	4.513	3
2	1.17	32.8	113.7	288.6	1.15	5.006	8.097	3	28	1.16	32.5	133.3	263.4	0.86	3.895	4.948	3
3	1.17	24.4	63.3	153.9	1.06	4.793	7.427	3	29	1.29	33.3	156.4	301.9	0.84	3.841	4.306	3
4	1.21	34.4	158.7	372.8	1.06	4.647	6.760	3	30	1.29	34.3	170.5	327.1	0.84	3.819	4.257	3
5	1.21	31.1	135.3	315.1	1.04	4.606	6.652	3	31	1.29	34.5	249.5	471.5	0.83	3.761	4.136	3
6	1.29	34.4	166.9	382.5	1.03	4.560	6.070	3	32	1.21	32.0	160.3	304.3	0.82	3.755	4.409	3
7	1.21	34.5	158.8	360.8	1.03	4.492	6.320	3	33	1.21	34.3	154.7	286.2	0.82	3.658	4.206	3
8	1.16	32.7	122.8	277.8	1.02	4.458	6.478	3	34	1.25	38.3	250.3	457.0	0.82	3.622	3.969	3
9	1.21	31.9	144.9	324.7	1.00	4.430	6.153	3	35	1.29	35.3	192.9	348.8	0.79	3.600	3.779	3
10	1.25	37.1	209.5	466.6	1.00	4.420	5.890	3	36	1.33	36.4	242.5	433.0	0.78	3.566	3.585	3
11	1.21	32.8	154.8	345.2	0.99	4.408	6.097	3	37	1.33	36.5	256.3	457.0	0.78	3.562	3.574	3
12	1.30	34.5	181.0	399.3	0.99	4.393	5.602	3	38	1.25	36.4	171.9	303.1	0.77	3.497	3.705	3 ⇄ 2
13	1.16	24.4	113.6	251.4	0.95	4.361	6.205	3	39	1.33	36.7	241.2	420.9	0.70	3.486	3.424	3 ⇄ 2
14	1.29	34.2	169.2	370.4	0.98	4.357	5.553	3	40	1.30	34.4	249.8	435.4	0.75	3.472	3.484	3 ⇄ 2
15	1.22	35.0	181.5	399.3	0.99	4.356	5.875	3	41	1.33	34.5	235.5	408.9	0.75	3.468	3.393	3 ⇄ 2
16	1.17	25.1	82.1	179.2	0.94	4.302	5.998	3	42	1.29	33.7	179.5	312.7	0.75	3.468	3.511	3 ⇄ 2
17	1.16	24.3	111.6	240.5	0.92	4.249	5.884	3	43	1.25	35.3	242.4	423.3	0.75	3.465	3.629	3 ⇄ 2
18	1.16	23.9	106.8	229.7	0.92	4.238	5.863	3	44	1.33	36.7	260.6	445.0	0.74	3.410	3.281	3 ⇄ 2
19	1.21	34.7	182.2	384.9	0.94	4.178	5.471	3	45	1.25	38.4	260.0	445.0	0.75	3.396	3.486	3 ⇄ 2
20	1.16	23.4	102.8	217.7	0.90	4.172	5.674	3	46	1.29	34.3	196.3	334.3	0.73	3.390	3.357	3 ⇄ 2
21	1.17	22.8	97.3	204.5	0.89	4.144	5.590	3	47	1.25	35.9	240.3	406.5	0.74	3.355	3.407	3 ⇄ 2
22	1.29	34.9	196.8	406.5	0.91	4.113	4.931	3	48	1.21	33.2	147.6	249.0	0.72	3.335	3.491	3 ⇄ 2
23	1.20	34.8	199.7	411.3	0.91	4.071	5.234	3	49	1.25	35.5	243.4	396.9	0.70	3.235	3.166	3 ⇄ 2
24	1.21	32.2	205.4	419.7	0.90	4.041	5.121	3	50	1.29	35.5	273.1	443.8	0.69	3.235	3.050	3 ⇄ 2
25	1.29	34.2	178.8	359.6	0.89	4.003	4.682	3	51	1.29	34.4	282.0	457.0	0.69	3.227	3.031	3 ⇄ 2
26	1.17	25.2	95.5	192.4	0.86	3.971	5.124	3	52	1.25	37.6	266.4	433.0	0.70	3.224	3.149	3 ⇄ 2

Table 2. (Continued.)

Run	p_{sat} (bar)	T_{in} (°C)	G (kg m^{-2} s^{-1})	q (kW m^{-2})	x_{out}	Bo $\times 10^3$	$K_1 \times 10^3$	Region	Run	p_{sat} (bar)	T_{in} (°C)	G (kg m^{-2} s^{-1})	q (kW m^{-2})	x_{out}	Bo $\times 10^3$	$K_1 \times 10^3$	Region
53	1.33	36.7	260.9	420.9	0.68	3.222	2.926	3 ⇄ 2	78	1.25	39.1	226.0	264.6	0.49	2.322	1.633	2
54	1.33	34.5	246.2	396.9	0.68	3.219	2.926	2	79	1.29	36.0	252.2	276.6	0.43	2.184	1.390	2
55	1.25	37.0	210.5	338.0	0.69	3.185	3.073	2	80	1.20	34.4	200.0	220.1	0.43	2.176	1.489	2
56	1.25	37.2	223.2	350.0	0.68	3.110	2.928	2	81	1.29	37.1	253.4	263.4	0.41	2.069	1.251	2
57	1.33	34.7	247.8	383.7	0.65	3.093	2.695	2	82	1.33	36.8	362.0	358.4	0.37	1.978	1.102	2
58	1.25	38.1	247.5	383.7	0.67	3.075	2.856	2	83	1.20	33.4	219.6	214.1	0.37	1.928	1.168	2
59	1.25	36.9	210.5	324.7	0.66	3.061	2.835	2	84	1.25	39.4	265.4	255.0	0.38	1.906	1.099	2
60	1.16	24.5	96.1	149.1	0.62	3.058	3.053	2	85	1.28	35.5	238.7	217.7	0.33	1.814	0.968	2
61	1.21	30.0	155.1	239.3	0.64	3.051	2.921	2	86	1.29	40.1	255.1	224.9	0.33	1.755	0.898	2
62	1.33	35.8	253.4	386.1	0.64	3.043	2.610	2	87	1.29	35.3	253.4	210.5	0.29	1.654	0.798	2
63	1.21	31.8	180.1	275.4	0.64	3.024	2.867	2	88	1.21	34.1	236.1	191.2	0.28	1.601	0.805	2
64	1.25	36.6	205.8	312.7	0.65	3.016	2.737	2	89	1.25	36.1	301.7	239.3	0.28	1.574	0.749	2
65	1.24	37.0	239.7	362.0	0.64	2.995	2.721	2	90	1.25	35.8	306.0	227.3	0.25	1.474	0.657	2 ⇄ 1
66	1.33	37.0	272.9	407.7	0.63	2.984	2.510	2	91	1.20	34.3	272.6	203.3	0.25	1.474	0.683	2 ⇄ 1
67	1.25	38.1	249.0	371.6	0.64	2.960	2.654	2	92	1.21	37.5	278.5	182.8	0.20	1.298	0.529	2 ⇄ 1
68	1.34	35.0	252.1	371.6	0.50	2.947	2.430	2	93	1.29	42.0	391.8	253.8	0.23	1.289	0.484	2 ⇄ 1
69	1.29	35.6	289.6	423.3	0.61	2.910	2.468	2	94	1.29	40.9	375.2	240.5	0.22	1.276	0.475	2 ⇄ 1
70	1.21	32.3	157.8	228.5	0.60	2.864	2.575	2	95	1.29	40.6	364.5	232.1	0.21	1.268	0.469	2 ⇄ 1
71	1.21	32.0	184.1	265.8	0.60	2.854	2.556	2	96	1.21	39.4	320.8	197.2	0.19	1.216	0.464	2 ⇄ 1
72	1.33	37.4	277.7	395.7	0.60	2.846	2.280	2	97	1.21	31.0	359.5	215.3	0.16	1.184	0.440	1
73	1.25	38.8	193.7	276.6	0.61	2.834	2.431	2	98	1.25	40.3	413.8	205.7	0.15	0.986	0.295	1
74	1.29	35.9	212.9	288.6	0.56	2.699	2.129	2	99	1.25	41.3	461.3	206.9	0.13	0.890	0.239	1
75	1.25	38.5	218.9	288.6	0.56	2.615	2.071	2	100	1.25	42.4	487.4	198.4	0.11	0.808	0.197	1
76	1.16	31.3	110.1	141.9	0.51	2.540	2.105	2	101	1.25	37.3	575.3	216.5	0.07	0.747	0.168	1
77	1.33	35.0	299.0	371.6	0.50	2.482	1.738	2	102	1.29	44.6	596.4	206.9	0.08	0.690	0.139	1

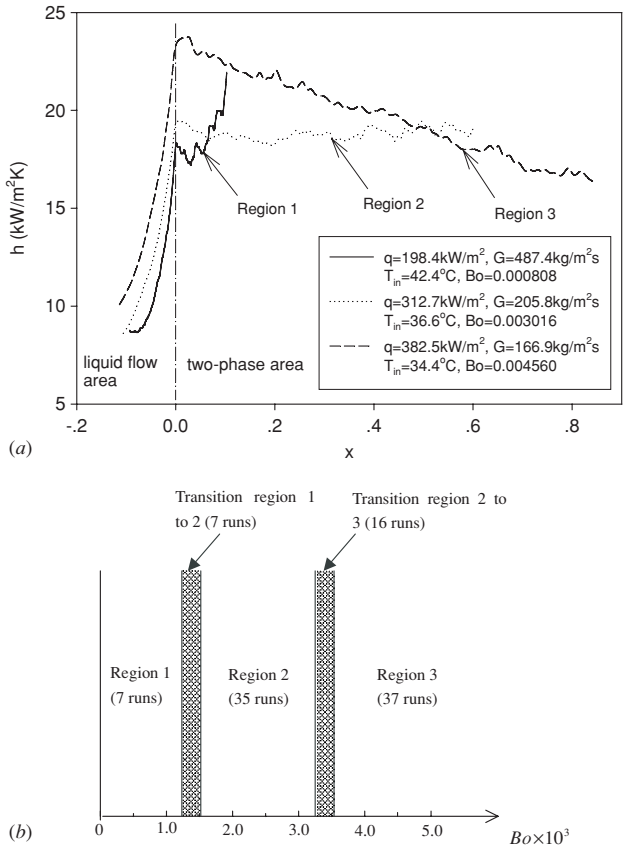

Figure 7. (*a*) Heat transfer coefficients versus the local vapor qualities and (*b*) the transition boundaries among the three heat transfer regions.

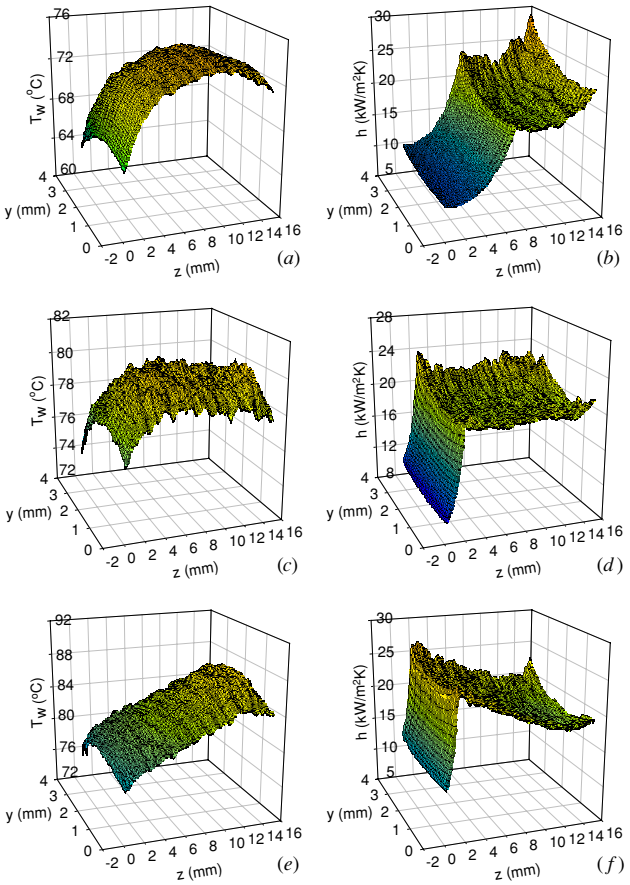

Figure 8. Spatial distributions of chip temperatures and heat transfer coefficients, (*a*), (*b*) $T_{in} = 42.4\ ^{\circ}$C, $G = 487.4$ kg m^{-2} s^{-1}, $q = 198.4$ kW m^{-2}, Bo $= 0.000\,808$, run 100; (*c*), (*d*) $T_{in} = 36.6\ ^{\circ}$C, $G = 205.8$ kg m^{-2} s^{-1}, $q = 312.7$ kW m^{-2}, Bo $= 0.003\,016$, run 64; (*e*), (*f*) $T_{in} = 34.4\ ^{\circ}$C, $G = 166.9$ kg m^{-2} s^{-1}, $q = 382.5$ kW m^{-2}, Bo $= 0.004\,560$, run 6.

illustrated in figure 7(*b*), in which there are seven runs for region 1, thirty-five runs for region 2 and thirty-seven runs for region 3. There are seven runs for the transition regions from 1 to 2, and sixteen runs from 2 to 3.

4.2. Two-dimensional chip temperature and heat transfer coefficient distributions

Figures 8(*a*)–(*b*), (*c*)–(*d*) and (*e*)–(*f*) illustrate the chip temperatures and heat transfer coefficients for low, medium and high boiling numbers, respectively. In all the runs, the microchannel entrance areas have *smooth, but increased* temperatures and the step increased heat transfer coefficients, due to these areas immersed by the liquid phase. However, in the two-phase areas, the spatial variations of these parameters are clearly seen, due to the liquid and vapor phases periodically flushing the microchannels alternately. The periodic flow displays random behavior for the specific locations. The side margins have slightly lower temperatures, due to the heat conduction effect of the silicon wall at the interface between the heated and the unheated area. The low and high boiling numbers lead to increased and decreased heat transfer coefficients along the flow direction, respectively, in the two-phase areas (see figures 8(*a*) and (*b*) and figures 8(*e*) and (*f*)). The microscale boiling heat transfer only shows nearly uniform temperature distributions along the flow direction at medium boiling numbers (see figures 8(*c*) and (*d*)). The transition boundaries among the three heat transfer regions are important in the chip design and operation. Quite uniform chip temperatures can be obtained with boiling numbers ranging from 1.574×10^{-3} to 3.219×10^{-3}. x_{out} ranges from 0.28 to 0.68. Uniform chip temperatures are useful to release the thermal stress and make the IC component work properly.

Further identification of the parameter distributions in the width direction can be seen from figure 9 for the same run as shown in figures 8(*e*) and (*f*). Generally the chip temperatures are slightly higher in the central areas and display a symmetric parabola distribution about $y = W/2$. The chip temperature differences across the whole width direction are less than 2 °C. Correspondingly, the heat transfer coefficients have the inverse distributions to the chip temperatures. The slight parabola distribution in the width direction is similar for the three heat transfer regions. It is noted that all the following figures present the parameters in the central area at $y = W/2$.

4.3. Measured heat transfer coefficients in the three heat transfer regions

Figure 10 presents the heat transfer coefficients versus x in region 1 for five runs. These five runs almost coincide with each other because there are smaller run parameter differences. Due to the lower Bo and x_{out}; the nucleate sites shift to the

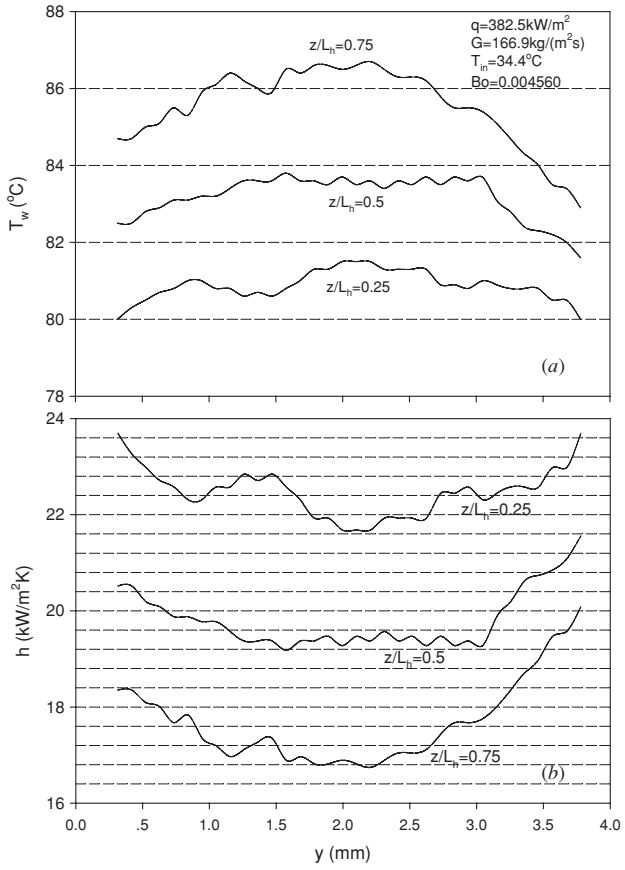

Figure 9. Variations of chip wall temperatures and heat transfer coefficients in the width direction for run 6.

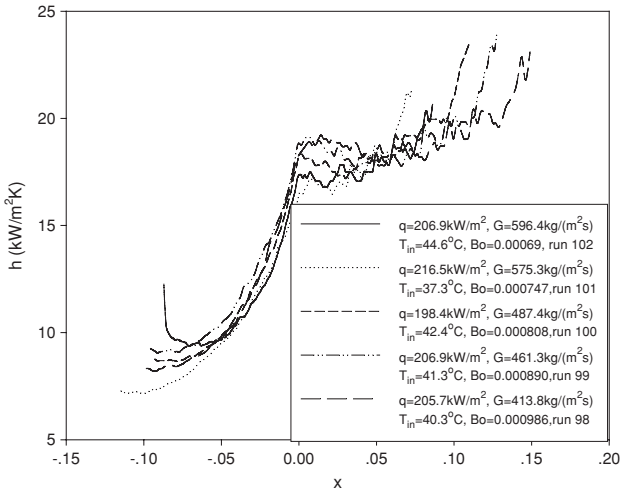

Figure 10. Heat transfer coefficients versus the thermodynamic vapor quality in region 1.

microchannel downstream, thus the heat transfer coefficients are increased at the end of heating area. Further studies are suggested in this region.

Figure 11 shows the heat transfer performances in region 2 for 12 runs, in which figures 11(*a*) and (*b*) indicate the heat flux effects with the mass fluxes fixed around 240 kg m^{-2} s^{-1} (figure 11(*a*) and 250 kg m^{-2} s^{-1} (figure 11(*b*), while figures 11(*c*) and (*d*) indicate the mass flux effects with

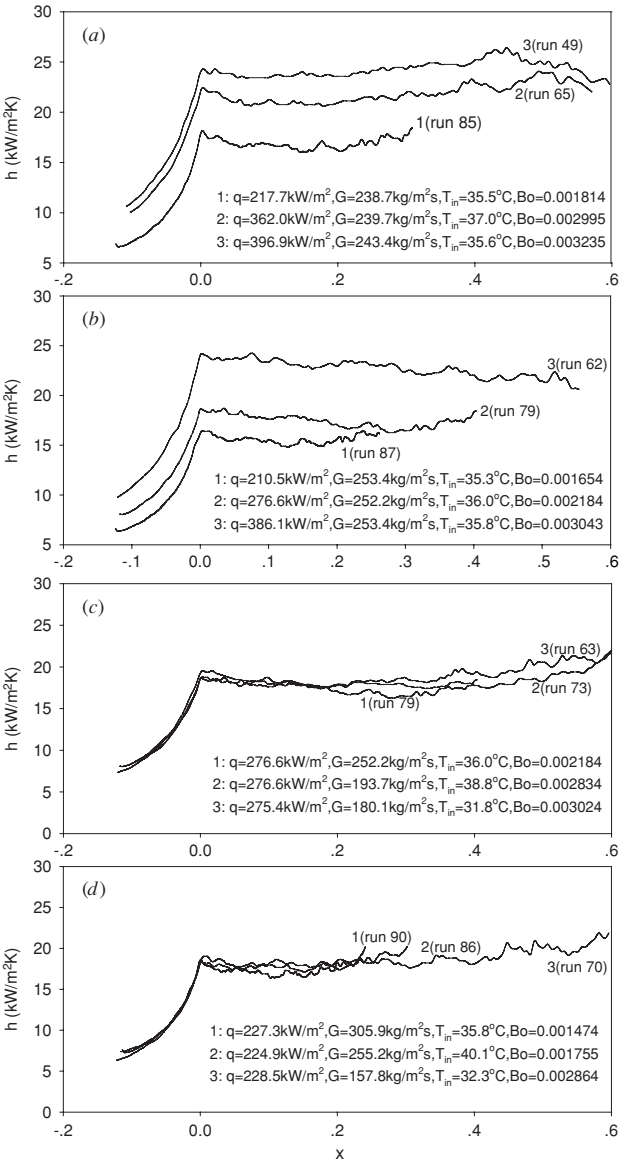

Figure 11. Effects of heat flux q and mass flux G on the heat transfer coefficients in region 2.

similar heat fluxes around 276 kW m^{-2} (figure 11(*c*)) and 225 kW m^{-2} (figure 11(*d*)). For all these runs, the heat transfer coefficients have nearly horizontal distributions versus the local vapor qualities. Clearly seen from figures 11(*a*) and (*b*) is the strong heat flux dependent on the heat transfer coefficients. Higher heat fluxes always induce higher heat transfer coefficients. Figures 11(*c*)–(*d*) provide strong experimental evidence that the mass fluxes have almost no effect on the heat transfer coefficients, behaving in the perfect 'nucleate boiling' controlled heat transfer mode. The forced convective heat transfer has neglected contributions. A physical explanation based on the transient flow patterns was given in section 3.4.

Figure 12 shows the heat transfer performances in region 3. Figure 12(*a*) is concerned with the heat flux effects with nearly constant mass flux within the very narrow range of 154.7–158.7 kg m^{-2} s^{-1}. It is seen from this figure that

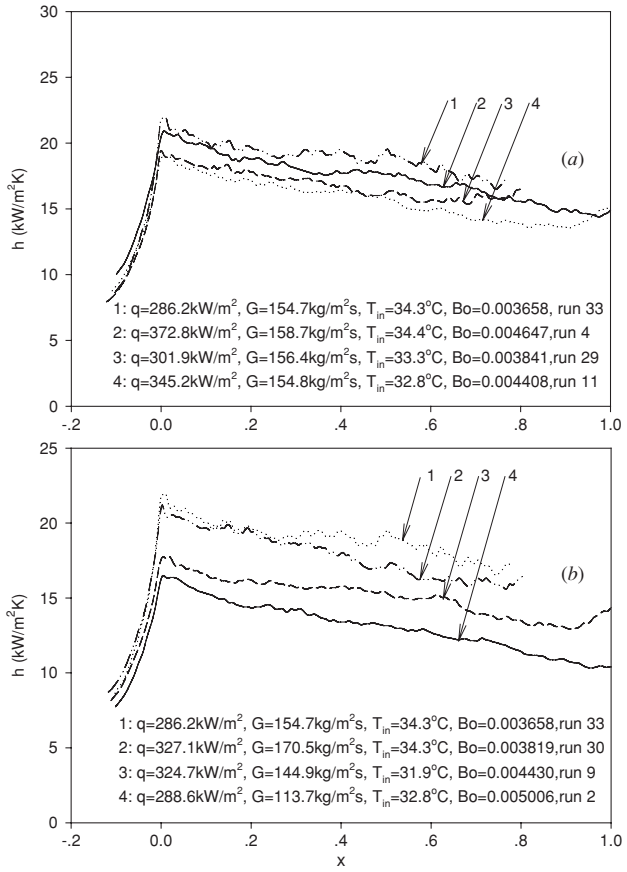

Figure 12. Effects of heat flux q and mass flux G on the heat transfer coefficients in region 3.

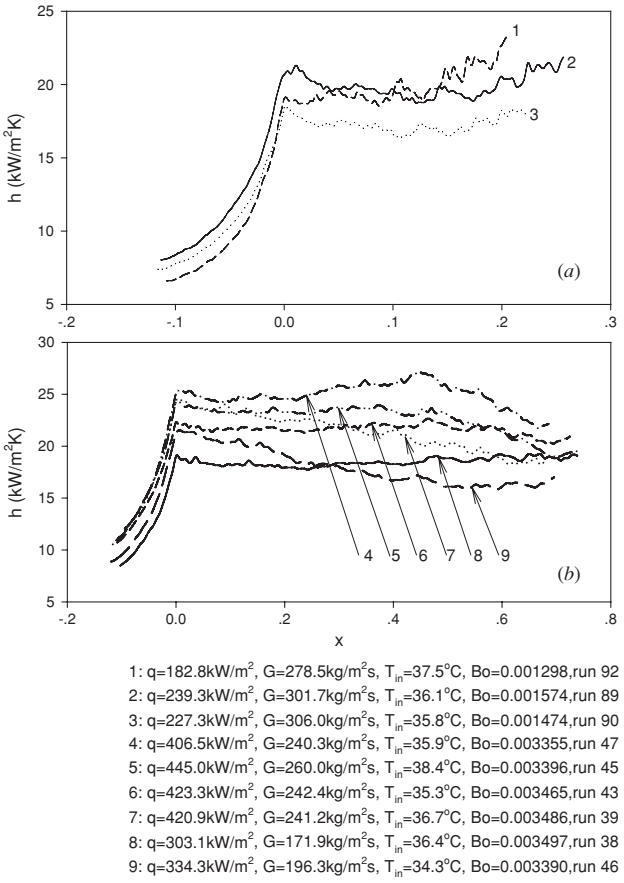

Figure 13. Effects of heat flux q and mass flux G on the heat transfer coefficients in the transition regions: (a) transition between regions 1 and 2, (b) transition between regions 2 and 3.

the heat transfer coefficients are less dependent on the heat fluxes. The four curves in figure 12(b) are divided into two groups: curves 1 and 4, and curves 2 and 3. The run for curve 1 has a higher mass flux of 154.7 kg m^{-2} s^{-1} than that of 113.7 kg m^{-2} s^{-1} for curve 4 when the heat fluxes are fixed around 287 kW m^{-2} for two runs, leading to higher heat transfer coefficients for curve 1. Similarly, the higher mass flux for curve 2 also yields higher heat transfer coefficients than that for curve 3. Generally for all these runs in region 3, the heat transfer coefficients are mainly dependent on the mass fluxes and decrease with increasing local vapor mass qualities. The heat fluxes have less influence. This phenomenon can be attributed to the high *bubble explosive induced forced convective heat transfer* mechanism under the high boiling numbers, as explained in section 3.4.

Finally we take a look at the measured heat transfer performances in the transition regions between 1 and 2 (see figure 13(a)), and between regions 2 and 3 (see figure 13(b)). The heat transfer coefficients display a horizontal followed by slightly increased distributions in the two-phase area for the boiling number of 0.001 298, behaving like the region 1 heat transfer mode to some extent. With slightly increasing the boiling number to 0.0014 74 or 0.001 574, the region 2 heat transfer mode (nucleate boiling heat transfer dominant) is fully established, with the heat transfer coefficients not dependent on the vapor mass qualities (see figure 13(a)). The transition region between regions 2 and 3 takes place within a very narrow range of boiling numbers from 3.222×10^{-3} to 3.497×10^{-3} (see figure 13(b)). Among these curves, the heat transfer coefficients were not dependent on the vapor mass qualities for curve 6 at Bo $= 3.465 \times 10^{-3}$ and curve 8 at Bo $= 3.497 \times 10^{-3}$ (nucleate boiling heat transfer mode), have constant followed by decreased distributions versus the local vapor mass qualities for curves 4 and 5, and transitions to the decreased heat transfer coefficients versus x for curves 7 and 9 (the bubble explosive induced forced convective heat transfer mode).

5. Comparisons with other studies and some discussions on microscale boiling heat transfer

In the authors' opinion, a full understanding of microscale boiling heat transfer needs both the flow pattern information and careful measurements of the heat transfer coefficients. Recently, high speed flow visualization techniques have been used by Jiang *et al* [11], Hetsroni *et al* [18] and Wu and Cheng [19]. Jiang *et al* [11] performed microscale boiling heat transfer experiments in microchannels with the hydraulic diameter as small as 26 μm. The flow patterns and temperature distributions were measured. The results are presented with the heat fluxes divided into low, medium and high regions. At low heat fluxes, few nucleation sites were observed. Medium heat flux yields the unstable slug flow and high heat flux

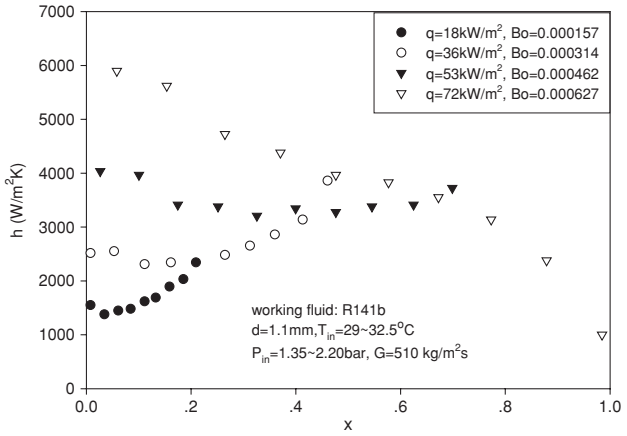

Figure 14. Effects of boiling numbers on the boiling heat transfer coefficients (data from Lin *et al* [24]).

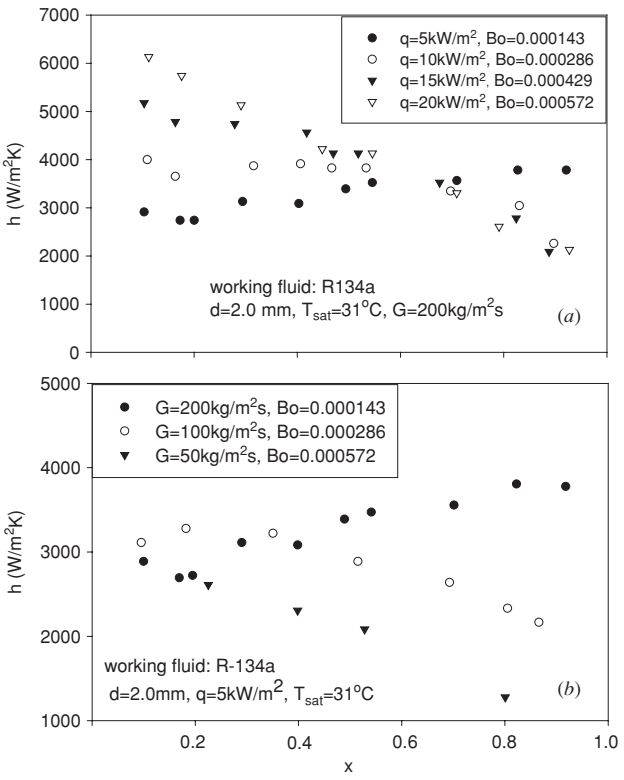

Figure 15. Effects of boiling numbers on the boiling heat transfer coefficients (data from Yan and Lin [9]).

results in the developed annular flow. Because the authors did not provide the heat transfer coefficient distributions versus the boiling numbers, direct comparisons between the present studies and their results may not be possible. Hetsroni *et al* [18] found that the low heat flux has the presence of a liquid phase in part of the microchannels. The high heat flux regime is characterized by convective boiling, in all parallel microchannels, accompanied by the quasi-periodic dry-out and refilling of the microchannels. Wu and Cheng [19] performed flow instability studies for microscale boiling heat transfer in silicon microchannels.

As stated in the introduction, a lot of miniature boiling heat transfer experiments were performed in capillary tubes. The heat transfer performances were evaluated by analyzing the heat transfer coefficients against the effects of heat fluxes, mass fluxes and vapor mass qualities. Lin *et al* [24] performed boiling heat transfer studies in 1 mm diameter tubes and discussed the boiling map for the mass flux of 510 kg m^{-2} s^{-1} and heat flux of 18–72 kW m^{-2} using R141b as the working fluid. Four curves are cited here for the local heat transfer coefficients versus the local vapor mass qualities in figure 14. The boiling numbers are increased gradually from 0.000 157 to 0.000 627. The heat transfer coefficients increase versus the vapor mass qualities at the smaller boiling numbers of 0.000 157 and 0.000 314 (region 1 mode), have nearly horizontal distributions versus x at the boiling number of 0.000 462 (region 2 mode) and decrease versus x at the high boiling number of 0.000 627 (region 3 mode), respectively. Figure 15 shows a set of heat transfer coefficients plotted versus x for the gradual increased boiling numbers by Yan and Lin [9]. Similar trends are found that the heat transfer coefficients could have increased, horizontal and decreased distributions versus x by increasing the boiling numbers.

Very recently, Lee and Mudawar [25] performed boiling heat transfer experiments in parallel copper microchannels with a heat flux of 15.9–93.8 W cm^{-2} and vapor mass qualities of 0.26–0.87. R134a is used as the working fluid. The heat transfer performances were evaluated on the basis of the vapor mass qualities and it was stated that they are associated with different heat transfer mechanisms for low, medium and high vapor qualities. Nucleate boiling occurs at the low qualities and high heat fluxes produce medium quality ($0.05 < x < 0.55$) or high quality ($x > 0.55$) annular film evaporation.

It is seen that the present studies in silicon microchannels qualitatively match the heat transfer performances in some capillary tubes or copper microchannels, with the boiling numbers or the vapor mass qualities as the control parameters.

Kandlikar [3] proposed the K_1 number (this number is strongly related to the boiling number), as a key to govern the microscale boiling heat transfer and concluded that 'heat transfer during flow boiling in microchannels is seen to be nucleate boiling dominant'. This conclusion is indeed valid for medium boiling numbers, but one should be careful in extending such a conclusion to high boiling numbers. As shown in the present paper, the experimental results can show forced convective heat transfer dominant at high boiling numbers. Under such conditions, the strong explosive induced forced convective heat transfer mechanism may suppress the nucleate boiling effect. Besides, the bubble nucleation sites shift to the microchannel upstream (relative local area behavior). Thus the heat transfer cannot be nucleate boiling dominant, but can be forced convective heat transfer as the major contribution. The present study may resolve the current conflict regarding nucleate boiling or forced convection heat transfer as the dominant mechanism.

Up to now little has been done on microscale boiling heat transfer modeling. Thome [17] presented numerical modeling based on the transient evaporation of thin liquid films surrounding the elongated bubbles. The flow patterns are coming from the adiabatic two-phase slug flow conducted in a 0.8 mm capillary tube. It is hoped that such a model can be modified to consider the five heat transfer mechanisms

deduced from the observed transient flow patterns, and the bubble explosion phenomenon, identified in the present paper.

6. Concluding remarks

This work provides a link between the transient flow patterns and the measured heat transfer coefficients in parallel microchannels. The following conclusions can be drawn:

1. In terms of the observed transient flow patterns in microchannels, five heat transfer mechanisms are identified: single-phase liquid forced convective heat transfer, nucleate boiling heat transfer, vapor explosive induced forced convective heat transfer, transient liquid film evaporation heat transfer and saturated or slightly superheated vapor heat transfer.
2. Because the transient flow patterns evolve so fast, the IR image system actually detects the time averaged temperatures. The probabilities of the four flow patterns and the liquid refilling for each microchannel satisfy the statistical principle. However, the IR image system can detect the spatial variations of the chip temperatures. Coupled with the silicon heat conduction between the heated and unheated areas, the center channel areas have slight higher temperatures and display symmetric parabola distributions at $y = W/2$ in the width direction. However, the maximum temperature difference across the width direction is less than 2 °C at high heat fluxes.
3. The boiling number establishes the relationship with the bubble nucleation locations and the exit vapor qualities. Other important information given by the boiling number is the evaporation momentum force relative to the inertia force. The probabilities of the bubble nucleation sites and the dry-out locations affect the heat transfer coefficient distributions along the flow direction.
4. At low boiling number, the bubble nucleation sites occur at the end of the heating area, resulting in increased heat transfer coefficients along the flow direction in the two-phase area. At medium boiling number, the bubble nucleation sites can occur anywhere. The transient process of a full cycle is similar to a successive process of bubble nucleation growth and departure followed by the fresh liquid refilling inside a cavity for a pool boiling situation. The measured heat transfer coefficients are dependent on the heat flux, not on the mass flux and the vapor qualities (nucleate boiling heat transfer mode).
5. At high boiling numbers, the bubble nucleation sites shift to the microchannel upstream and partial or full dry-out may occur at the end of the heating area, leading to decreased heat transfer coefficients with increasing local vapor qualities. The bubble explosion results in high evaporation momentum force, suppressing the inertia force. The measured heat transfer coefficients mainly rely on the mass fluxes, less on the heat fluxes, attributed to the bubble explosive induced forced convective heat transfer mechanism.
6. The transition criteria among the three heat transfer regions are given. Based on the present study, a uniform chip temperature field could be acquired by selecting suitable boiling number ranges, which is useful for high heat flux chip temperature control. Further works are suggested using different working fluids. The conflicting conclusions (either nucleate boiling heat transfer dominant or forced convective heat transfer dominant) drawn by different authors maybe attributed to the different parameter ranges or the experimental instrumentation.

Acknowledgments

This work is supported by the National Natural Science Foundation of China (10272102), Natural Science Foundation of Guangdong Province (32700) and the Science and Technology Development Foundation of Guangdong Province (33103).

References

[1] Kandlikar S G 2002 Fundamental issues related to flow boiling in minichannels and microchannels *Exp. Therm. Fluid Sci.* **26** 389–407
[2] Thome J R 2004 Boiling in microchannels: a review of experiment and theory *Int. J. Heat Fluid Flow* **25** 128–39
[3] Kandlikar S G 2004 Heat transfer mechanisms during flow boiling in microchannels, ASME *J. Heat Transfer* **126** 8–16
[4] Lazarek G M and Black S H 1982 Evaporative heat transfer, pressure drop and critical heat flux in a small vertical tube with R-113 *Int. J. Heat Mass Transfer* **25** 945–60
[5] Wambsganss M W, France D M, Jendrzejczyk J A and Tran T N 1993 Boiling heat transfer in a horizontal small-diameter tube *ASME, J. Heat Transfer* **115** 963–72
[6] Tran T N, Wambsganss M W and France D M 1996 Small circular and rectangular-channel boiling with two refrigerants *Int. J. Multiph. Flow* **22** 485–98
[7] Kew P A and Cornwell K 1997 Correlations for the prediction of boiling heat transfer in small-diameter channels *Appl. Therm. Eng.* **17** 705–15
[8] Ravigururajan T S 1998 Impact of channel geometry on two-phase flow heat transfer characteristics of refrigerants in microchannel heat exchangers *ASME, J. Heat Transfer* **120** 485–91
[9] Yan Y and Lin T 1998 Evaporation heat transfer and pressure drop of refrigerant R-134a in a small pipe *Int. J. Heat Mass Transfer* **41** 4183–94
[10] Bao Z Y, Fletcher D F and Haynes B S 2000 Flow boiling heat transfer of Freon R11 and HCFC123 in narrow passages *Int. J. Heat Mass Transfer* **43** 3347–58
[11] Jiang L, Wong M and Zohar Y 2001 Forced convection boiling in a microchannel heat sink *J. Microelectromech. Syst.* **10** 80–7
[12] Lee H J and Lee S Y 2001 Heat transfer correlation for boiling flows in small rectangular horizontal channels with low aspect ratios *Int. J. Multiph. Flow* **27** 2043–62
[13] Hetsroni G, Mosyak A, Segal Z and Ziskind G 2002 A uniform temperature heat sink for cooling of electronic devices *Int. J. Heat Mass Transfer* **45** 3275–86
[14] Warrier G R, Pan T and Dhir V K 2002 Heat transfer and pressure drop in narrow rectangular channels *Exp. Therm. Fluid Sci.* **26** 53–64
[15] Yu W, France D M, Wambsganss M W and Hull J R 2002 Two-phase pressure drop, boiling heat transfer, and critical heat flux to water in a small-diameter horizontal tube *Int. J. Multiph. Flow* **28** 927–41
[16] Qu W and Mudawar I 2003 Flow boiling heat transfer in two-phase micro-channel heat sinks —I. Experimental investigation and assessment of correlation methods *Int. J. Heat Mass Transfer* **46** 2755–71
[17] Thome J R, Dupont V and Jacobi A M 2004 Heat transfer model for evaporation in microchannels Part 1. Presentation of the model *Int. J. Heat Mass Transfer* **47** 3375–85

[18] Hetsroni G, Mosyak A, Segal Z and Pogrebnyak E 2003 Two-phase flow patterns in parallel microchannels *Int. J. Multiph. Flow* **29** 341–60

[19] Wu H Y and Cheng P 2003 Visualization and measurements of periodic boiling in silicon microchannels *Int. J. Heat Mass Transfer* **46** 2603–14

[20] Xu J L, Gan Y H, Zhang D C and Li X H 2005 Microscale boiling heat transfer in a micro-timescale at high heat fluxes *J. Micromech. Microeng.* **15** 362–76

[21] Bennett G A and Briles S D 1989 Calibration procedure developed for IR surface-temperature measurements *IEEE Trans. Compon. Hybrids Manuf. Technol.* **12** 690–5

[22] Zhang X M, Xu J L and Zhou Z Q 2004 Experimental study of a pulsating heat pipe using FC-72, ethanol, and water as working fluids *Exp. Heat Transfer* **17** 47–67

[23] Yaws C L 1999 *Chemical Properties Handbook* (New York: McGraw-Hill)

[24] Lin S, Kew P A and Cornwell K 2001 Two-phase heat transfer to a refrigerant in a 1.1 mm diameter tube *Int. J. Refrig.* **24** 51–6

[25] Lee J and Mudawar *et al* 2005 Two-phase flow in high heat flux microchannel heat sink for refrigeration cooling applications: part II. Heat transfer characteristics *Int. J. Heat Mass Transfer* **48** 941–55